

SI-BEARING MOLECULES TOWARD IRC+10216: ALMA UNVEILS THE MOLECULAR ENVELOPE OF CWLEO

L. VELILLA PRIETO^{1,2}, J. CERNICHARO¹, G. QUINTANA-LACACI¹, M. AGÚNDEZ¹, A. CASTRO-CARRIZO³, J. P. FONFRÍA⁴, N. MARCELINO⁵, J. ZÚÑIGA⁶,
A. REQUENA⁶, A. BASTIDA⁶, F. LIQUE⁷ AND M. GUÉLIN^{3,8}

Submitted 2015 April 8 — Published in ApJL 2015 May 27

ABSTRACT

We report the detection of SiS rotational lines in high-vibrational states as well as SiO and SiC₂ lines in their ground vibrational state toward IRC+10216 during the Atacama Large Millimeter Array Cycle 0. The spatial distribution of these molecules shows compact emission for SiS and a more extended emission for SiO and SiC₂, and also proves the existence of an increase in the SiC₂ emission at the outer shells of the circumstellar envelope. We analyze the excitation conditions of the vibrationally excited SiS using the population diagram technique, and we use a large velocity gradient model to compare with the observations. We found moderate discrepancies between the observations and the models that could be explained if SiS lines detected are optically thick. Additionally, the line profiles of the detected rotational lines in the high energy vibrational states show a decreasing linewidth with increasing energy levels. This may be evidence that these lines could be excited only in the inner shells, i.e., the densest and hottest, of the circumstellar envelope of IRC+10216.

Subject headings: astrochemistry — circumstellar matter — line: identification — molecular processes — stars: AGB and post-AGB — stars: individual (IRC+10216)

1. INTRODUCTION

Silicon is mostly locked in SiS, SiO and SiC₂ in the circumstellar envelope (CSE) of the carbon-rich star IRC+10216, as evidenced observationally and predicted by models (Olofsson et al. 1982; Lucas et al. 1995; Agúndez et al. 2012). These molecules are efficiently formed in the gas phase, close to the stellar photosphere as a consequence of chemical processes enabled under thermodynamical equilibrium (Tsuji 1973). In the dust formation region ($\sim 5\text{--}20 R_*$), the Si-bearing molecules are likely to condense onto the dust grains due to their highly refractory nature. The silicon contained in the dust grains can form molecules through grain-surface reactions. Also, the interaction of shocks produced by the pulsation of the star with the dust grains can extract certain amounts of silicon from the grains and incorporate that silicon into the gas-phase to react and form other species (see e.g. Castro-Carrizo et al. 2001). Beyond this region, the abundances of Si-bearing molecules are expected to decrease up to the outermost shells of the envelope, where the interstellar ultraviolet (UV) radiation field dissociates all the remaining molecules.

Previous interferometer observations showed the spatial distribution of these molecules in IRC+10216. The SiS $J=5-4$, $J=6-5$, $J=8-7$, $J=9-8$ and $J=12-11$ bright-

ness distributions display a quasi-circular shape with a diameter of $\sim 20''$ elongated along the nebular axis (P.A. $\sim 20^\circ$, Bieging & Tafalla 1993; Lucas et al. 1995). Recent observations with the Combined Array for Research in Millimeter-wave Astronomy (CARMA) of the SiS $J=14-13$ $v=0$ and $v=1$ lines have been reported by Fonfría et al. (2014), where the $v=0$ line shows a circular and compact brightness distribution of $\sim 2''$ and displays maser emission. The $v=1$ brightness distribution shows a compact source centered at the star position.

SiO $J=5-4$ $v=0$ brightness distribution maps carried out with the Submillimeter Array (SMA) were reported in Schöier et al. (2006). They show circular symmetry with a diameter of $\sim 6''$ at the systemic velocity of the source, which is -26.5 km s^{-1} (e.g. Cernicharo et al. 2000). The $J=6-5$ $v=0$ brightness distribution reported in Fonfría et al. (2014) displays a quasi-circular symmetry centered at the position of the star, with a diameter of $\sim 3''$ elongated along the nebular direction (NE–SW).

SiC₂ observations carried out with the Plateau de Bure Interferometer (PdBI) and CARMA, show a brightness distribution composed of: (i) an elongated compact component located at the innermost regions of the CSE (Fonfría et al. 2014) and, (ii) a hollow shell structure located at $\sim 15''$ from the star (Lucas et al. 1995). The formation mechanism for this outer component was suggested in Cernicharo et al. (2010), where the reaction between Si and C₂H₂ yielding SiC₂, could be responsible for the SiC₂ enhancement in the outer envelope.

In this work we present the Cycle 0 observations carried out with the Atacama Large Millimeter Array (ALMA) toward IRC+10216. We detected emission of SiS $J=15-14$ lines of vibrationally excited states, from $v=0$ up to $v=7$, and tentatively of $v=8$, 9 and 10. $J=15-14$ lines of different isotopologues are also detected: ²⁹SiS ($v=0-5$), ³⁰SiS ($v=0-4$), Si³³S ($v=0-3$), Si³⁴S ($v=0-4$), ²⁹Si³³S ($v=0$) and ²⁹Si³⁴S ($v=0$). We also detected emission of SiO $J=6-5$ ($v=0-2$), ²⁹SiO $J=6-5$ ($v=0$) and several lines of SiC₂ in the ground vibrational state.

¹ Group of Molecular Astrophysics. ICMM, CSIC. C/ Sor Juana Inés de la Cruz 3, 28049 Cantoblanco, Madrid, Spain

² Centro de Astrobiología, INTA–CSIC. E-28691 Villanueva de la Cañada, Madrid, Spain

³ Institut de Radioastronomie Millimétrique. 300 rue de la Piscine, F-38406, Saint Martin d'Hères, France

⁴ Departamento de Estrellas y Medio Interestelar, Instituto de Astronomía, Universidad Nacional Autónoma de México (UNAM). Ciudad Universitaria, 04510, Mexico City, México

⁵ Istituto di Radiastronomia, INAF–CNR, via Gobetti 101, 40129 Bologna, Italy

⁶ Departamento de Química Física, Facultad de Química, Universidad de Murcia. Campus Espinardo, 30100 Murcia, Spain

⁷ LOMC–UMR 6294, CNRS–Université du Havre, 25 rue Philippe Lebon, BP. 1123, 76063 Le Havre cedex, France

⁸ LERMA, Observatoire de Paris, PSL Research University, CNRS, UMR 8112, F-75014, Paris, France

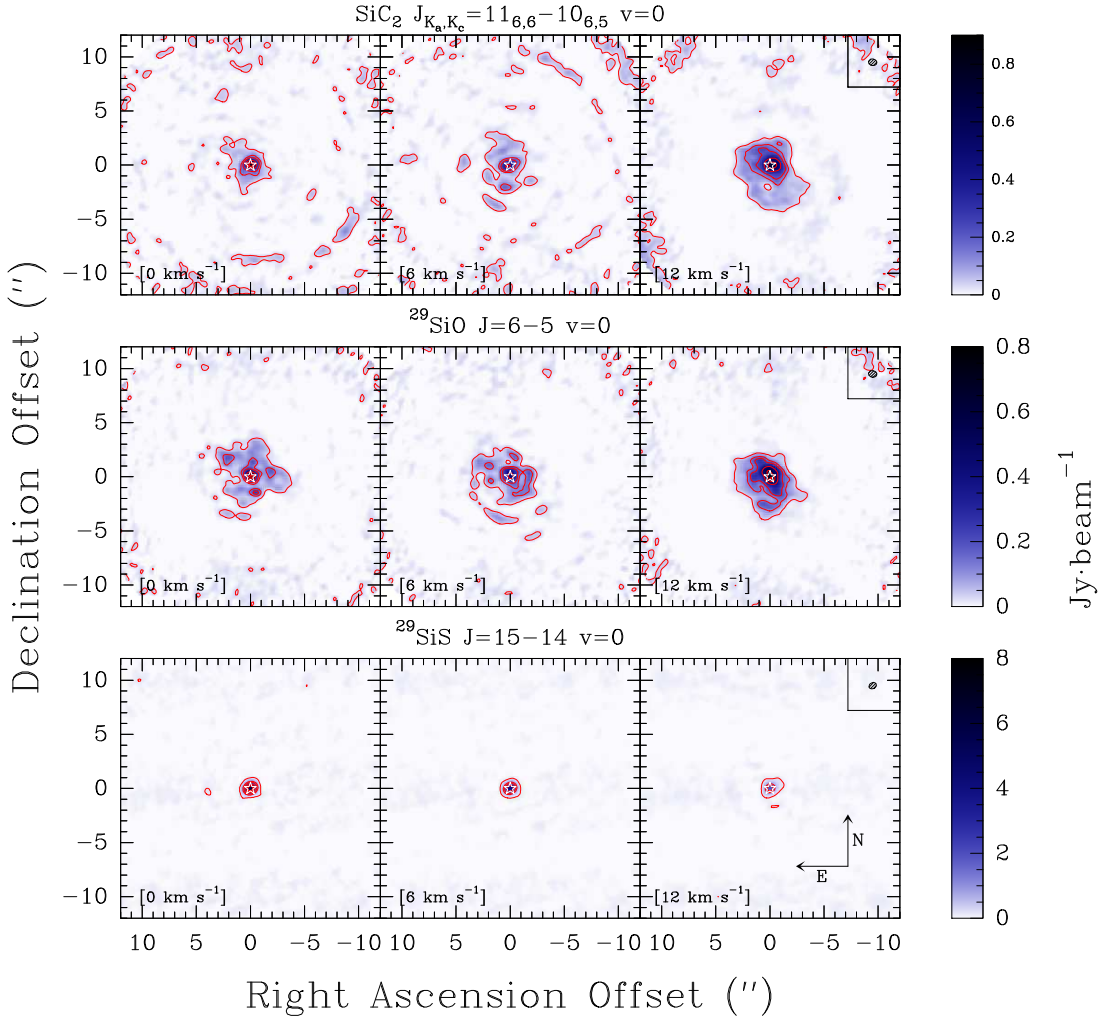


FIG. 1.— From top to bottom: SiC_2 $J_{K_a, K_c}=11_{6,6}-10_{6,5}$ $v=0$, ^{29}SiO $J=6-5$ $v=0$ and ^{29}SiS $J=15-14$ $v=0$. Three velocity offsets with respect to the V_{LSR} of the source are shown: +0, +6 and +12 km s^{-1} . The position of the star is shown as a white star. The first contour corresponds to 5σ (see Table 1) and the rest correspond to 15, 25, 50, 75 and 90% of the maximum intensity, except for ^{29}SiS $J=15-14$ where the first contour is at 25σ level (a large-scale artificial modulation appears below that level). The synthetic beam is represented in the top right corner of each of the three maps series. The intensity scale in Jy beam^{-1} is shown at the right edge of the figure. The orientation is explicitly shown in the bottom right box.

2. OBSERVATIONS

The observations were carried out with ALMA⁹ between 2012 April 8 and 23 during Cycle 0. IRC+10216 was observed in the frequency range 255.3 to 274.8 GHz (band 6) covered by four different setups with a bandwidth of ~ 5 GHz, a channel spacing of 0.49 MHz and an effective resolution of 0.98 MHz. Detailed information of each setup is summarized in Table 1. The observations were performed using sixteen antennas covering baselines up to 402 m that allowed us to obtain an angular resolution of $\sim 0.6''$. The shortest baselines used were ~ 20 m which allow us to recover structures with a size up to $\lesssim 12''$. Two runs of 72 minutes each were performed, of which 26 minutes correspond to correlations on source. Further details about calibration and imaging restora-

tion can be found in Cernicharo et al. (2013). The coverage of the uv plane achieved with the setup 6 provides low contributions of the sidelobes ($\leq 10\%$ of the primary beam) to the dirty beam. For the rest of the setups the uv coverage is worse and large contributions of the sidelobes (up to 20–30% of the primary beam) appear in the dirty beam.

The continuum comes from a point-like source located at $\alpha=9^{\text{h}}47^{\text{m}}57^{\text{s}}.446$ and $\delta=13^{\circ}16'43''.86$ (J2000), which is in good agreement with the position of IRC+10216 measured with the Very Large Array (VLA) with 40 mas resolution (Menten et al. 2012). We measured an intensity peak of 650 mJy beam^{-1} with an uncertainty of $\sim 8\%$.

The calibration of the data was performed using CASA¹⁰ and data analysis with GILDAS¹¹.

⁹ This paper makes use of the following ALMA data: ADS/JAO.ALMA#2011.0.00229.S. ALMA is a partnership of ESO (representing its member states), NSF (USA) and NINS (Japan), together with NRC (Canada), NSC and ASIAA (Taiwan), and KASI (Republic of Korea), in cooperation with the Republic of Chile. The Joint ALMA Observatory is operated by ESO, AUI/NRAO and NAOJ.

¹⁰ CASA (Common Astronomy Software Applications) is a comprehensive software package used to calibrate, image, and analyze radioastronomical data from interferometers. See: <http://casa.nrao.edu>

¹¹ GILDAS is a worldwide software mainly used to process, reduce, and analyze astronomical single-dish and interferometric observations. It is maintained by the Institut de Radioastronomie Millimétrique (IRAM). See: <http://www.iram.fr/IRAMFR/GILDAS>

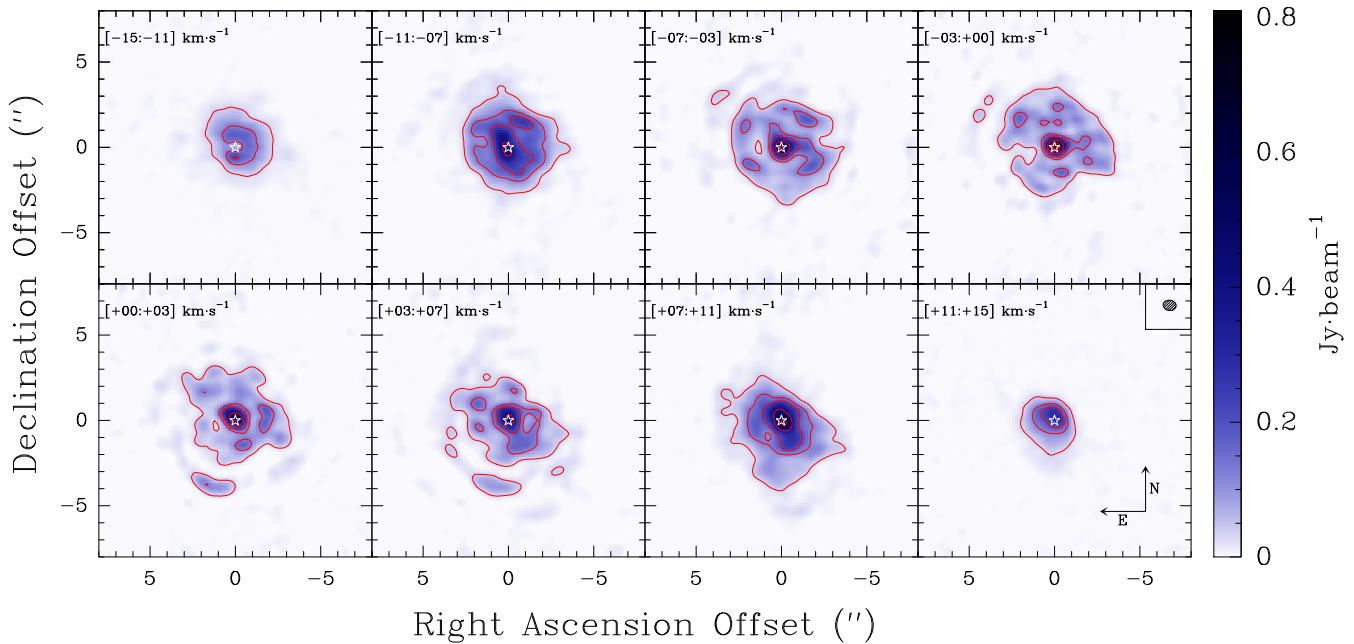


FIG. 2.— $^{29}\text{SiO } J=6-5 \ v=0$ velocity interval averaged maps. The velocity averaged interval is shown at the top left corner of each box. These velocities are offset velocities with respect to the V_{LSR} of the source (-26.5 km s^{-1}). The position of the star is shown as a white star. The first contour corresponds to 5σ (see Table 1) and the rest correspond to 15, 25, 50, 75 and 90% of the maximum intensity. The intensity scale in Jy beam^{-1} is shown at the right edge of the figure. The synthetic beam is represented in the top right corner of the bottom right box. The orientation is explicitly shown in the bottom right box.

TABLE 1
OBSERVATIONAL PARAMETERS.

Setup #	Frequency range (GHz)	RMS (mJy beam^{-1})	Synthetic beam ($'' \times ''$)	FOV [†] ($''$)
3	269.9–274.8	6	0.61×0.47	23.2–22.9
4	265.0–269.9	10	0.86×0.47	23.7–23.2
5	260.2–265.0	17	0.96×0.47	24.2–23.7
6	255.3–260.2	6	0.77×0.60	24.6–24.2

NOTE. — [†]Field of view calculated as $\theta(\text{rad})=1.22\lambda(\text{mm})/D(\text{mm})$, where D is the diameter of a single antenna (12 m) and λ is the observed wavelength.

3. RESULTS

3.1. Spatial distribution of Si-bearing molecules

In Figs. 1 and 2, we show maps of the emission of the lines $\text{SiC}_2 J_{K_a, K_c}=11_{6,5}$, $^{29}\text{SiO } J=6-5$ and $^{29}\text{SiS } J=15-14$ in their ground vibrational state at different offset velocities with respect to the systemic velocity of the source.

SiC_2 (Fig. 1) displays a central component elongated in the NE–SW direction with a size of $\sim 4\text{--}5''$ along the nebular axis and $\sim 3\text{--}4''$ in the perpendicular direction. The elongation is also observed in the ^{29}SiO emission (see below) and in the SiO and SiC_2 maps by Fonfría et al. (2014) where the authors invoke a possible bipolar outflow to explain it. At the systemic velocity of the source and at $+6 \text{ km s}^{-1}$ offset, a ring-like, clumpy and weak component is seen at $\sim 10\text{--}11''$ from the central star. The angular distance between the position of the star and the ring structure, considering a distance of $\sim 130 \text{ pc}$ to the star from us (Groenewegen et al. 2012), corresponds to a linear distance of $\sim 2 \times 10^{16} \text{ cm}$. This ringlike component is consistent with the peak abundance of SiC_2 in the outer envelope of IRC+10216 reported in Lucas et al. (1995) and the chemical model of Cernicharo et al. (2010). Although, this ringlike structure is probably filtered in our data given the shortest baselines used. Between the central and the ringlike structure, emission of SiC_2 is either very low or absent (Lucas et al. 1995). Finally, the redshifted emission

($+12 \text{ km s}^{-1}$) displays a quasi-circular distribution with a diameter of $\sim 5\text{--}6''$. These brightness distributions could be interpreted as the SiC_2 is formed in regions close to the star, then it condenses onto the dust grains, and eventually it reappears at the outer shells of the CSE, perhaps as a hollow shell, as the consequence of the interaction between the UV Galactic radiation field and the CSE (Lucas et al. 1995; Fonfría et al. 2014).

For ^{29}SiO (Figs. 1 and 2), the bulk of the emission arises from a compact central component with a size of $2''$. This line also displays an extended and clumpy distribution, elongated in the NE–SW and with a size of $\sim 6\text{--}7''$. At velocities close to the terminal expansion velocity, $\sim 14.5 \text{ km s}^{-1}$ (Cernicharo et al. 2000), the brightness distribution is elongated in the NE–SW direction with a size of $\sim 3\text{--}4''$. The blueshifted emission at -13 km s^{-1} displays a decrease just in front of the star, which can be interpreted as self-absorption and probably absorption of the continuum emission mostly coming from the star. There is no conclusive explanation for the elongation; nevertheless, some authors pointed out that it could evidence the presence of a bipolar outflow in the CSE (Fonfría et al. 2014). The possible presence of a binary companion to CWLeo could also play a decisive role in this scenario (Guelin et al. 1993; Cernicharo et al. 2015).

The observed brightness distributions of the vibrationally excited SiS lines are expected to be compact and centered on the star since the involved levels are excited at the high temperatures prevailing close to the star. The $\text{SiS } J=15-14 \ v=0$ line, which displays maser emission (Fonfría Expósito et al. 2006), shows a circular brightness distribution with a diameter of $\sim 2''$ at the systemic velocity of the source. For the $\text{SiS } J=15-14 \ v \geq 1$ lines, the observed distributions are not spatially resolved. Fig. 1 shows the emission of the $^{29}\text{SiS } J=15-14 \ v=0$ line, which displays a brightness distribution of a compact source surrounding the central star with a diameter

of $\sim 2''$. A large-scale artificial modulation can be seen below the 25σ level. Since it is related to the visibilities at short baselines, we do not expect it to modify the shape and flux of the compact central component of the brightness distribution. Also, the quality of the several SiS and ^{29}SiS maps is affected owing to the low uv coverage and non-negligible contribution of the sidelobes for the setups 3–5 (see Table 1). The lines that lie in the range covered by the setup 6, are those of high vibrationally excited states (e.g. SiS $J=15-14$ $v \geq 10$, ^{29}SiS $J=15-14$ $v \geq 6$) which are tentative and spatially unresolved.

3.2. Vibrationally excited SiS

The Cycle 0 observations with ALMA allowed us to detect several $J=15-14$ lines of high vibrationally excited states of SiS isotopologues, in particular, up to $v=7$ for the main isotopologue (see Fig. 3). The SiS $J=15-14$ $v=8$ and $v=10$ lines are probably blended with unidentified lines, so we consider them to be tentative. Additionally, the SiS $J=15-14$ $v=9$ line is considered tentatively detected because even though its FWHM measured seems to follow the trend shown in Fig. 3, its measured integrated intensity is underestimated considering the population diagram of Fig. 3. All these lines display a compact unresolved emission peaking at the central star. The FWHM of the lines measured from the spectra at the stellar position decreases with increasing upper level energy (see Fig. 3). We verified this behavior for SiS, ^{29}SiS , ^{30}SiS , Si^{33}S and Si^{34}S . In the dust formation region, the gas displays a velocity gradient as a function of the radial distance to the star, i.e., the closer to the star the lower the expansion velocity (Agúndez et al. 2012, and references therein). Hence, those lines involving higher vibrational states, which are excited in inner and warmer regions, are narrower. Thermal broadening for the SiS lines excited in the dust formation region is $\sim 1 \text{ km s}^{-1}$, and thus this mechanism could only account partially for the FWHM variation of the lines.

We analyzed the excitation conditions of SiS with the rotational diagram technique (Goldsmith & Langer 1999) using the spectra at the stellar position (see Fig. 3). We considered two different linear trends for the observational data: one for the transitions with $E_{up} \lesssim 2500 \text{ K}$ (i.e. $v=0, 1$ and 2), and a different trend for the rest (i.e. $v=3-7$). The $v \geq 8$ lines are excluded from the fit. The values derived from the $v=0$ to $v=2$ fit are uncertain owing to the maser nature of the SiS $J=15-14$ $v=0$ line and also due to possible optically thick emission. Both data series show a linear behavior consistent with a single vibrational (excitation) temperature for each of the fits. The vibrational temperature derived from the fit involving the transitions in high-energy vibrational states is higher than the temperature derived for the low vibrational levels. Therefore, the emission produced by SiS transitions in high-energy vibrational states can only arise from regions close to the photosphere. This result is similar to the one obtained by Cernicharo et al. (2011) for HCN.

We used a large velocity gradient (LVG) code to model the SiS emission (Cernicharo 2012). Further details about the spectroscopic data used in the calculations are given in § 3.2.1. The SiS collisional data were taken from Toboła et al. (2008) and extrapolated to high rovibrational levels. We adopted a distance to the star of $\sim 130 \text{ pc}$, an effective temperature of $\sim 2330 \text{ K}$ and a stellar radius of $\sim 4 \times 10^{13} \text{ cm}$ as input for our model (Cernicharo et al. 2000; Monnier et al. 2000; Groenewegen et al. 2012). We used two different models: (i) the model of Agúndez et al. (2012), which was used to reproduce the molecular abundances in the inner layers

of IRC+10216, that we call the “2012 model”, and, (ii) this work, which is a modification of the model (i). We modified the H_2 density, decreasing it by a factor ~ 2 , as described in Cernicharo et al. (2013) (this was used to reproduce the dust nucleation zone, $1-10 R_*$, of IRC+10216). Additionally, the SiS abundance in the dust nucleation zone needs to be balanced with a similar increase (factor of ~ 2) to avoid an underestimation of the SiS emission. From these models (see Fig. 3) we obtain a good agreement with the vibrational temperature derived from the vibrational diagram and moderate discrepancies with the total column density within a factor of ~ 2 . These discrepancies in the column density may be explained by the dilution due to the size of the emitting region compared to the half power beam width of the synthetic beam, which would increase the optical depth of the lines. The size of the emitting region should decrease with the vibrational state owing to the energies needed to excite those lines. With our models, we found moderate to high optical depths $\tau(v=1) \sim 10$ to $\tau(v=4) \sim 0.8$ for the abundance profile (i) and $\tau(v=1) \sim 47$ to $\tau(v=8) \sim 1.0$ for the abundance profile (ii).

3.2.1. SiS potential energy function and vibrational dipole moment

The potential energy function used to describe the internuclear motions of the SiS isotopologues is a Born–Oppenheimer (BO) potential properly extended to accommodate Born–Oppenheimer breakdown (BOB) corrections. The effective potential has the form (Campbell et al. 1993; Ram et al. 1997; Dulick et al. 1998; Coxon & Hajigeorgiou 2000)

$$V^{eff}(r) = V^{BO}(r) + \frac{V_A(r)}{M_A} + \frac{V_B(r)}{M_B} - \frac{\hbar^2}{2\mu} [1 + q(r)] \frac{J(J+1)}{r^2} \quad (1)$$

where M_A and M_B are the silicon and sulfur atomic masses and μ is the reduced mass. The BO potential is given by

$$V^{BO}(r) = D_e \left[\frac{1 - e^{-\beta(r)}}{1 - e^{-\beta(\infty)}} \right]^2 \quad (2)$$

where

$$\beta(r) = z \sum_{i=0}^4 \beta_i z^i \quad (3)$$

$$\beta(\infty) = \sum_{i=0}^4 \beta_i \quad (4)$$

and

$$z = \frac{r - r_e}{r + r_e} \quad (5)$$

and the BOB potential and centrifugal correction terms are represented by the power expansions

$$V_A(r) = \sum_{i=1}^4 u_i^A z^i \quad (6)$$

$$V_B(r) = \sum_{i=1}^4 u_i^B z^i \quad (7)$$

$$q(r) = M_A^{-1} \sum_{i=1}^4 q_i^A z^i + M_B^{-1} \sum_{i=1}^4 q_i^B z^i \quad (8)$$

The potential parameters were obtained by nonlinear least squares fitting to the observed infrared and microwave line

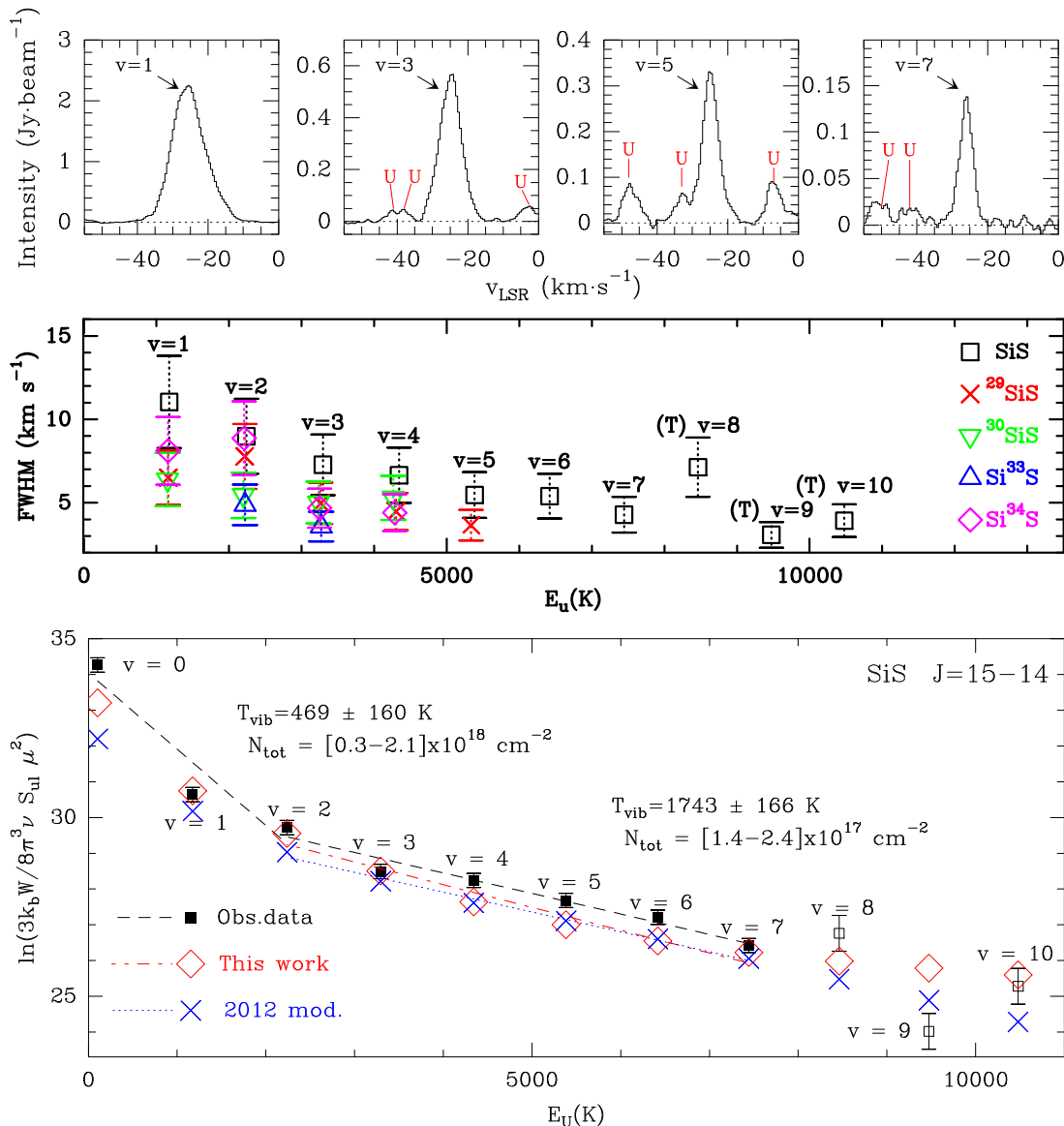


FIG. 3.— (Top) Central pixel spectra of the SiS $J=15-14$ $v=1, 3, 5$ and 7 lines. Unidentified lines are marked with an U. Baselines are indicated in each box with a dashed line. (Middle) FWHM of the $v \geq 1$ detected lines of SiS isotopologues in the central pixel versus the upper energy of the transition. The tentative lines are marked with a (T). We adopted a 25% value of the total measure for the uncertainties, which takes into account uncertainties of the calibration, statistical errors, and the contribution of the sidelobes of the dirty beam. (Bottom) Vibrational diagram of the SiS $J=15-14$ lines. The vibrational quantum number of each line is shown. The errorbars represent a 20% of the integrated intensity of the line and a 50% for the $v=8, 9$ and 10 lines. The values derived for the vibrational temperature and column density are shown with their formal errors for two fits: $v=0-2$ and $v=3-7$. The LVG models (see § 3.2) are plotted with a rhombus and a cross.

positions of the SiS isotopologues up to $v=12$. The final data set included a total of 2863 lines, 414 rotational transitions (Tieinan et al. 1972; Sanz et al. 2003; Müller et al. 2007) and 2449 rovibrational transitions (Birk et al. 1972; Frum et al. 1990). Mass-independent Dunham coefficients, U_{ij} , have been derived by Müller et al. (2007). The fit to the potential energy function was performed using the Levenberg–Marquardt algorithm (Levenberg 1944; Marquardt 1963) to minimize the χ^2 function, with the line positions weighted by the square of the experimental uncertainties. The rovibrational energy levels of the isotopologues needed to calculate the line positions were computed by solving the radial Schrödinger equation using the variational method of Harris et al. (1965) along with harmonic-type basis functions. The potential parameters obtained in the fit are given in the comments of the Table 2. The final

χ^2 value was 1.767. The unweighted standard deviations for the rotational and, vibrational-rotational line positions were 0.0229 MHz and 0.000657 cm $^{-1}$, respectively.

The dipole moment function used for SiS was determined semiempirically by Piñeiro et al. (1987), and the dipole moment matrix elements were computed up to $v=4$. In Table 2 we provide them up to $v=12$. The agreement between our calculations and those of Piñeiro et al. (1987) for $v \leq 4$ is excellent.

3.3. Other Si-bearing species

SiC was detected in IRC+10216 by Cernicharo et al. (1989) with line profiles indicating that the molecule was produced in an external shell, probably as a product of the photodissociation of SiC $_2$. Our observations did not cover any frequency range where SiC lines could arise; however, lines of

^{29}SiC and $\text{SiC } v=1$ lie in this range, but they were not detected. For a temperature in the photosphere of 2300 K a significant number of SiC molecules could be in the $v=1$ state ($E_{\text{up}} \sim 1400$ K) and higher vibrational levels. We derived an upper limit to the SiC column density of $4.4 \times 10^{14} \text{ cm}^{-2}$ from the ^{29}SiC upper limit, where we used an isotopic $^{28}\text{Si}/^{29}\text{Si}$ ratio of 20 (Cernicharo et al. 1989, 1991). Hence, SiC_2 is the main carrier of SiC bonds in the gas phase in the dust formation zone of IRC+10216.

4. CONCLUSION

ALMA has proved to be an outstanding tool to study the molecular emission from CSEs of evolved stars, even at the early stages of its development. In particular, ALMA allowed us to detect SiS rotational lines in high-energy vibrational states that have been analyzed to constrain the physical con-

ditions of the innermost shells of IRC+10216. We found that these lines should be excited in regions close to the photosphere of IRC+10216. It also has served to unveil the different brightness distributions of Si-bearing molecules. We expect that future ALMA science, with its full suite of capabilities ready for the next observation cycle, would give us the chance to map the brightness distributions of these Si-bearing molecules in greater detail, allowing us to understand their formation mechanisms.

We thank the Spanish MINECO/MICINN for funding support through grants AYA2009-07304, AYA2012-32032, the ASTROMOL Consolider project CSD2009-00038 and the European Research Council (ERC Grant 610256: NANOCOSMOS).

REFERENCES

- Agúndez, M., Fonfría, J. P., Cernicharo, J., et al. 2012, *A&A*, 543, AA48
 Biegging, J. H., & Tafalla, M. 1993, *AJ*, 105, 576
 Birk H., and Jones H., 1972, *Chem. Phys. Lett.* 175, 536.
 Campbell, J. M., Dulick, M., Klapstein, D., et al., 1993, *J. Chem. Phys.*, 99, 8379
 Castro-Carrizo, A., Lucas, R., Bujarrabal, V., Colomer, F., & Alcolea, J. 2001, *A&A*, 368, L34
 Cernicharo, J., Gottlieb, C. A., Guelin, M., Thaddeus, P., & Vrtilik, J. M. 1989, *ApJ*, 341, L25
 Cernicharo, J., Guelin, M., Kahane, C., Bogey, M., & Demuynck, C. 1991, *A&A*, 246, 213
 Cernicharo, J., Guélin, M., & Kahane, C. 2000, *A&AS*, 142, 181
 Cernicharo, J., Waters, L. B. F. M., Decin, L., et al. 2010, *A&A*, 521, LL8
 Cernicharo, J., Agúndez, M., Kahane, C., et al. 2011, *A&A*, 529, LL3
 Cernicharo, J. 2012, *EAS Publications Series*, 58, 251
 Cernicharo, J., Daniel, F., Castro-Carrizo, A., et al. 2013, *ApJ*, 778, LL25
 Cernicharo, J., Marcelino, N., Agúndez, M., & Guélin, M. 2015, *A&A*, 575, AA91
 Coxon, J. A., and Hajigeorgiou, P. G., 2000, *J. Mol. Spectrosc.*, 203, 49
 Dulick, M., Zhang, K. Q., Guo, B., and Bernath, P. F., 1998, *J. Mol. Spectrosc.*, 188, 14
 Fonfría Expósito, J. P., Agúndez, M., Tercero, B., Pardo, J. R., & Cernicharo, J. 2006, *ApJ*, 646, L127
 Fonfría, J. P., Fernández-López, M., Agúndez, M., et al. 2014, *MNRAS*, 445, 3289
 Frum C.I., Engleman Jr. R., Bernath P.F., 1990, *J. Chem. Phys.*, 93, 5457
 Goldsmith, P. F., & Langer, W. D. 1999, *ApJ*, 517, 209
 Groenewegen, M. A. T., Barlow, M. J., Blommaert, J. A. D. L., et al. 2012, *A&A*, 543, LL8
 Guelin, M., Lucas, R., & Cernicharo, J. 1993, *A&A*, 280, L19
 Harris, D. O., Engerholm, G. G., and Gwinn, W. D., 1965., *J. Chem. Phys.*, 43, 1515
 Levenberg, K., 1944, *Quart. Appl. Math.*, 2, 164
 Lucas, R., Guélin, M., Kahane, C., Audinos, P., & Cernicharo, J. 1995, *Ap&SS*, 224, 293
 Marquardt, D. W., 1963, *J. Soc. Ind. Appl. Math.*, 11, 431
 Menten, K. M., Reid, M. J., Kamiński, T., & Claussen, M. J. 2012, *A&A*, 543, AA73
 Monnier, J. D., Danchi, W. C., Hale, D. S., et al. 2000, *ApJ*, 543, 861
 Morris, M., Gilmore, W., Palmer, P., Turner, B. E., & Zuckerman, B. 1975, *ApJ*, 199, L47
 Müller, H.S.P., McCarthy, M.C., Bozzocchi, L., et al., 2007, *Chem. Phys. Phys. Chem.*, 9, 1579
 Olofsson, H., Johansson, L. E. B., Hjalmarsen, A., & Nguyen-Quang-Rieu 1982, *A&A*, 107, 128
 Piñeiro, A. L. L., Tipping, R. H., and Chackerian, J. C., 1987, *J. Mol. Spectrosc.*, 125, 184
 Ram, R. S., Dulick, M., Guo, B., et al., 1997, *J. Mol. Spectrosc.*, 183, 360
 Sanz M.E., McCarthy M.C., Thaddeus P., 2003, *J. Chem. Phys.*, 119, 11715
 Schöier, F. L., Fong, D., Olofsson, H., Zhang, Q., & Patel, N. 2006, *ApJ*, 649, 965
 Tiemann E., Renwanz E., Hoefft J., Torring T., 1972, *Z. Naturforsch.* 27a, 1566
 Toboła, R., Lique, F., Kłos, J., & Chafasiński, G. 2008, *Journal of Physics B Atomic Molecular Physics*, 41, 155702
 Tsuji, T. 1973, *A&A*, 23, 411

TABLE 2
CALCULATED VIBRATIONAL DIPOLE MOMENT MATRIX ELEMENTS (D) FOR $^{28}\text{Si}^{32}\text{S}$.

v'/v''	0	1	2	3	4	5	6	7	8	9	10	11	12
0	1.7420												
1	-0.1348	1.7658											
2	-0.6333×10^{-2}	-0.1907	1.7896										
3	0.4068×10^{-3}	0.1101×10^{-1}	0.2336	1.8135									
4	-0.3379×10^{-4}	-0.8184×10^{-3}	-0.1564×10^{-1}	0.2697	1.8375								
5	-0.3359×10^{-5}	-0.7613×10^{-4}	-0.1302×10^{-2}	0.2027×10^{-1}	-0.3016	1.8615							
6	0.3804×10^{-6}	-0.8306×10^{-5}	0.1329×10^{-3}	-0.1852×10^{-2}	-0.2493×10^{-1}	0.3304	1.8857						
7	0.4752×10^{-7}	0.1018×10^{-5}	0.1569×10^{-4}	-0.2046×10^{-3}	0.2465×10^{-2}	0.2961×10^{-1}	-0.3568	1.9100					
8	-0.6394×10^{-8}	-0.1363×10^{-6}	-0.2061×10^{-5}	0.2587×10^{-4}	-0.2916×10^{-3}	-0.3137×10^{-2}	0.3433×10^{-1}	0.3814	1.9343				
9	-0.9087×10^{-9}	-0.1952×10^{-7}	-0.2934×10^{-6}	0.3612×10^{-5}	-0.3918×10^{-4}	-0.3943×10^{-3}	0.3866×10^{-2}	0.3909×10^{-1}	-0.4045	1.9587			
10	0.1339×10^{-9}	0.2936×10^{-8}	0.4441×10^{-7}	-0.5435×10^{-6}	0.5779×10^{-5}	0.5594×10^{-4}	-0.5130×10^{-3}	-0.4649×10^{-2}	0.4388×10^{-1}	0.4262	1.9833		
11	0.2005×10^{-10}	0.4562×10^{-9}	0.7033×10^{-8}	-0.8654×10^{-7}	0.9143×10^{-6}	0.8674×10^{-5}	-0.7649×10^{-4}	-0.6482×10^{-3}	0.5485×10^{-2}	0.4871×10^{-1}	-0.4469	2.0079	
12	-0.2954×10^{-11}	-0.7182×10^{-10}	-0.1147×10^{-8}	0.1437×10^{-7}	-0.1525×10^{-6}	-0.1437×10^{-5}	0.1241×10^{-4}	0.1011×10^{-3}	-0.8003×10^{-3}	-0.6373×10^{-2}	0.5358×10^{-1}	0.4667	2.0326

NOTE. — Internuclear potential energy parameters for the SiS molecule: $D_e=51993.7274 \text{ cm}^{-1}$, $r_e=1.929260274 \text{ \AA}$, $\beta_0=5.9671641$, $\beta_1=5.8793706$, $\beta_2=9.3200373$, $\beta_3=18.402479$, $\beta_4=18.451287$, $u_1^{\text{Si}}=-749.1309 \text{ cm}^{-1} \text{ amu}$, $u_2^{\text{Si}}=6844.274 \text{ cm}^{-1} \text{ amu}$, $u_1^{\text{S}}=-1003.321 \text{ cm}^{-1} \text{ amu}$, $u_2^{\text{S}}=7128.960 \text{ cm}^{-1} \text{ amu}$.